Highly Asymmetric Electrolytes in the Primitive Model: Hypernetted Chain Solution in Arbitrary Spatial Dimensions

Marco Heinen,*[a] Elshad Allahyarov,[a,b] and Hartmut Löwen[a]

The pair-correlation functions for fluid ionic mixtures in arbitrary spatial dimensions are computed in hypernetted chain (HNC) approximation. In the primitive model (PM), all ions are approximated as nonoverlapping hyperspheres with Coulomb interactions. Our spectral HNC solver is based on a Fourier-Bessel transform introduced by Talman (J. Comput. Phys. 1978, 29, 35), with logarithmically spaced computational grids. Numeric efficiency for arbitrary spatial dimensions is a commonly exploited virtue of this transform method. Here, we highlight another advantage of logarithmic grids, consisting in efficient sampling of pair-correlation functions for highly asymmetric ionic mixtures. For three-dimensional fluids, ion size and charge-ratios larger than 1000 can be treated, corresponding to hitherto computationally not accessed micrometer-sized colloidal spheres in 1-1 electrolyte. Effective colloidal charge numbers are extracted from our PM results. For moderately large ion size and charge-asymmetries, we present molecular dynamics simulation results that agree well with the approximate HNC pair correlations. © 2013 Wiley Periodicals, Inc.

DOI: 10.1002/jcc.23446

Introduction

Most of the essential features of polyelectrolyte solutions can be efficiently modeled by a combination of charges and excluded volume, see[1–4] for reviews. In the so-called primitive model (PM), all specific properties of the solvent are neglected except for its dielectric constant. Research over the past decades has shown that some of the basic properties of polyelectrolytes (like screening and Coulomb association) are contained in the asymmetric PM of electrolytes which enables wide applications to charged colloidal suspensions, micelles and globular proteins. However, for high asymmetry in charge and size between the microions and macroions, as occurring in suspensions of charged colloidal particles, the PM is not easy to solve numerically in general. For example, structural correlations in the PM were obtained by numerically expensive computer simulations only up to charge and diameter asymmetries of about 1:100,[5–10] corresponding to the micellar rather than the colloidal regime.

In this article, liquid structure is computed by solving integral equations based on the Ornstein-Zernike (OZ) equation.[11] This approach requires an approximative closure for an explicit solution. A rather simple but successful closure is the hypernetted chain (HNC) scheme,[12] which has been proven to be a realistic approximation for mixtures of charged particles. The numerical solution methods presented here can be straightforwardly generalized to more sophisticated, thermodynamically partially self-consistent OZ closure relations[13–15] like, for example, the one proposed by Zerah and Hansen.[16] For the sake of simplicity, and as it was shown that enforcing thermodynamic self-consistency leads to a weak accuracy improvement only,[17] in the present work we restrict ourselves to the HNC approximation. A variety of liquid integral equation[17–23] or density functional studies[24–26] of the PM have been reported. The HNC equations have been solved for the asymmetric PM by Léger and Levesque,[27] in case of nonzero macroion number densities for size asymmetries between microions and macroions as high as 1:80 and charge asymmetries ranging up to 1:450.

The HNC scheme can be formulated in any spatial dimension $d > 0$. While $d = 3$ is the standard three-dimensional situation, it is important to note that also two-dimensional and one-dimensional fluids occur in experiments with strong confinement between glass plates or at interfaces, or in one-dimensional channels.[28] Dimensions higher than $d = 3$ have no immediate realization. However, they play an important role in constructing and testing theories and are also helpful to find suitable mean-field-like approximations in lower dimensions.[29–32] Hence, there is a need to study charged systems also in $d > 3$. We formulate the solution method in this article for arbitrary $d > 0$, with explicit data presented for spatial dimensions $d = 1, 2, 3, 4, 5$, and 6.

[a] M. Heinen, E. Allahyarov, H. Löwen
Institut für Theoretische Physik II, Weiche Materie, Heinrich-Heine-Universität, Düsseldorf, 40225 Düsseldorf, Germany
E-mail: mheinen@thphy.uni-duesseldorf.de

[b] E. Allahyarov
Theoretical Department, Joint Institute for High Temperatures, Russian Academy of Sciences (IVTAN), 13/19 Izhorskaya street, Moscow 125412, Russia

Contract grant sponsor: European Research Council (ERC) Advanced Grant INTERCOCOS; Contract grant number: FP7 Ref.-Nr. 267499

Here we pick up a strategy of solving the PM-HNC equations that, for $d = 3$, has first been used by Rossky and Friedman.[33] The key idea lies in using computational grids with logarithmic spacing in coordinate- and wavenumber space. For even number of dimensions d, in particular for $d = 2$, the use of logarithmic grids in a spectral OZ equation solver emerges as a necessary consequence of mapping the occurring Fourier-Bessel transforms to numerically efficient fast Fourier transform (FFT) methods.[34–38] Hence, logarithmic grids appear quite naturally in $d = 2$ liquid integral equation studies like, for example, Refs. 39,40. For odd number of dimensions, where FFT methods can be applied directly on uniformly spaced grids, using logarithmic grids is a less obvious approach which has nevertheless been used in some $d = 3$ studies.[41–43] In none of these studies, however, extensive use has been made of an important virtue of the logarithmic grids, which is highlighted in our present article. The simultaneous dense distribution of grid points at very different length scales renders logarithmic grids ideal for the discretization of pair-correlation functions in a highly asymmetric PM, at moderate numerical expense. Here we are presenting results for ion size and charge-asymmetries as high as 1:1000 (both asymmetries simultaneously reached, for nondilute suspensions), which represents well the colloidal regime. To our knowledge, no liquid integral equation or computer simulation studies have been published so far, where asymmetries of this magnitude have been reached.

We investigate the accuracy of the HNC pair-correlation functions by comparing to results of numerically expensive molecular dynamics (MD) simulations, for ion charge- and diameter asymmetries up to 1:500 and 1:250, respectively. The HNC results are found to be in overall good agreement with the MD results, except for a somewhat underestimated principal peak in the macroion radial distribution function at high macroion charge numbers.

Our results can be used to extract colloidal effective interaction potentials, including nonsaturated effective charge numbers, at high-numerical efficiency. As opposed to other approximate theories for colloidal effective charge numbers like the cell model (CM)[44,45] or the renormalized jellium model (RJM),[9,10,46–51] pair correlations among all ionic species are treated on equal footing in our method, with the HNC entering as the only approximation. The virtue of the CM and RJM, conversely, is their applicability in larger ranges of salt concentrations and macroion charge numbers.

In a future study, the method described here could be augmented to include colloidal surface chemistry, described by a mass action balance that takes into account the local variations in the pH value near the colloidal surfaces. This would allow for parameter free *ab initio* calculation of pair correlations in colloidal suspensions with reactive electrolyte like, for example, suspensions of silica spheres in NaOH with a re-entrant fluid-crystal-fluid phase diagram, reported in Refs. 52,53.

Methodology

The *d*-dimensional PM

Let n_i, with $1 \leq i \leq m$, denote the number density of ions of species i in an m-component fluid mixture of hyperspherical particles in an arbitrary positive number d of spatial dimensions. Then, $n = \sum_i n_i$ is the total particle number density and $\chi_i = n_i/n$ is the mole fraction of species i. Let $Z_i e$ denote the electric charge of a particle of species i, where e is the elementary charge. In order to prevent singular attractions between oppositely charged particles, ions of species i possess a hard-core diameter σ_i. Hence, the particles of species i occupy a fraction

$$\varphi_i = V(d)(\sigma_i/2)^d n_i \tag{1}$$

of the system hypervolume, where $V(d) = \pi^{d/2}/\Gamma(d/2+1)$ is the d-dimensional unit hypersphere volume, $\Gamma(x)$ denoting the Gamma function. All ions are assumed neutrally buoyant in an infinite structureless solvent, which is fully described by the solvent dielectric constant ε in the PM applied here. We express all real-space functions in units of the dimensionless particle-center to particle-center distance $x = rn^{1/d}$.

The functions $u_{ij}(x) = V_{ij}(x)/(k_B T)$ are the pair-potentials of direct interaction, $V_{ij}(x)$, between ions of species i and j, divided by the Boltzmann constant k_B and the absolute temperature T. The dimensionless pair-potentials can be decomposed as

$$u_{ij}(x) = u_{ij}^{(s)}(x) + u_{ij}^{(l)}(x) \tag{2}$$

into short-ranged (hard-core) parts

$$u_{ij}^{(s)}(x) = \begin{cases} \infty & \text{for } x < \sigma_{ij} n^{1/d}, \\ 0 & \text{otherwise}, \end{cases} \tag{3}$$

with pairwise additive hard core diameters $\sigma_{ij} = (\sigma_i + \sigma_j)/2$, and long-ranged (Coulomb) parts

$$u_{ij}^{(l)}(x) = \begin{cases} -\Gamma_{ij} \ln(x) & \text{for } d = 2, \\ \dfrac{\Gamma_{ij}}{(d-2)x^{d-2}} & \text{for } d \neq 2, \end{cases} \tag{4}$$

with coupling constants $\Gamma_{ij} \propto Z_i Z_j$. In $d = 3$ dimensions, connection to experimentally accessible systems can be made by choosing the coupling constant Γ_{ij} in eq. (4) as $\Gamma_{ij} = L_B n^{1/3} Z_i Z_j$, involving the solvent-specific Bjerrum length $L_B = e^2/(\varepsilon k_B T)$ in Gaussian units. In this article, we investigate only such systems that obey the Berthelot mixing rule $\Gamma_{ij}^2 = \Gamma_{ii}\Gamma_{jj}$.[54]

One-component systems, $m = 1$, with pair-potential according to eqs. (2)–(4), are commonly referred to as (d-dimensional) one component plasmas (OCPs). Global electroneutrality of an OCP implies the presence of a homogeneous background charge density that does not couple to the distribution of the correlated ions (like, for example, an electron plasma at sufficiently high temperature). For systems with $m > 1$ components, global electroneutrality without a neutralizing charge background is enforced in all cases studied here, by requiring that $\sum_i n_i Z_i = 0$.

HNC scheme

We compute the ion pair-correlations in the PM described in the previous section, by numerically solving the OZ equations[11] in combination with the approximate HNC closure.[12–14] In an isotropic, homogeneous fluid mixture, the coupled OZ equations may be written as

$$\gamma_{ij}(x)=\chi_k\int d^d\mathbf{x}'\,c_{ik}(x')[c_{kj}(x-x')+\gamma_{kj}(x-x')]. \tag{5}$$

In eq. (5) and the rest of this article, we adhere to the Einstein summation convention. Equation (5) can be regarded as the definitions of the partial direct correlation functions $c_{ij}(x)$ in terms of the continuous partial indirect correlation functions $\gamma_{ij}(x)=h_{ij}(x)-c_{ij}(x)=g_{ij}(x)-1-c_{ij}(x)$. The latter identity comprises the total correlation functions $h_{ij}(x)$ and the partial radial distribution functions (rdf's), $g_{ij}(x)$, which are the conditional probabilities of finding a particle of species j at a dimensionless center-to-center distance x from a particle of species i.[11] Note here that various labels have been attributed to the indirect correlation functions in the literature. Apart from the symbol $\gamma(x)$ used here, common notations are $t(x)$[55] and $b(x)$.[11]

An isotropic function f can be Fourier-transformed in d dimensions as

$$\tilde{f}(y)=\frac{(2\pi)^{d/2}}{y^{d/2-1}}\int_0^\infty dx\,x^{d/2}f(x)J_{d/2-1}(xy), \tag{6}$$

$$f(x)=\frac{x^{1-d/2}}{(2\pi)^{d/2}}\int_0^\infty dy\,y^{d/2}\tilde{f}(y)J_{d/2-1}(xy), \tag{7}$$

with $J_n(x)$ denoting the Bessel function of the first kind and order n. Using the convolution theorem, the OZ equations are Fourier-transformed into the space of dimensionless wavenumbers y, where they read

$$\tilde{\gamma}_{ij}(y)=\chi_k\tilde{c}_{ik}(y)\tilde{c}_{kj}(y)+\chi_k\tilde{c}_{ik}(y)\tilde{\gamma}_{kj}(y). \tag{8}$$

The OZ equations need to be supplemented by an appropriate closure relation. The HNC closure, which is known to be a good approximation for the PM,[17] reads

$$c_{ij}(x)=\exp\{\gamma_{ij}(x)-u_{ij}(x)\}-\gamma_{ij}(x)-1. \tag{9}$$

Numerical solution of the set of eqs. (5) and (9) in combination with the long-ranged potentials in eqs. (2)–(4) requires splitting the analytically known long-ranged asymptotic parts $\mp u_{ij}^{(l)}(x)$ off the direct and indirect correlation functions as[11,27,56]

$$c_{ij}(x)=c_{ij}^{(s)}(x)-u_{ij}^{(l)}(x) \tag{10}$$

and

$$\gamma_{ij}(x)=\gamma_{ij}^{(s)}(x)+u_{ij}^{(l)}(x). \tag{11}$$

The so-defined functions $c_{ij}^{(s)}(x)$ and $\gamma_{ij}^{(s)}(x)$ are considerably shorter in range than $c_{ij}(x)$ and $\gamma_{ij}(x)$. We note here that eq. (11) is a simple but suboptimal choice of defining a short-ranged part of the indirect correlation function. The so-defined functions $\gamma_{ij}^{(s)}(x)$ decay exponentially, but less steeply than the functions $c_{ij}^{(s)}(x)$. An indirect correlation function part that is short-ranged in a stricter sense than $\gamma_{ij}^{(s)}(x)$ used here, is obtained in a renormalized formulation based on the diagrammatic expansion[11] of the correlation functions,[55,57–59] where a chain sum of $u_{ij}^{(l)}(x)$, instead of $u_{ij}^{(l)}(x)$ itself is subtracted off the function $\gamma_{ij}(x)$. However, the decay of $\gamma_{ij}^{(s)}(x)$ defined in eq. (11) is steep enough for our purposes, which is largely owed to our use of logarithmic grids that extend to very large values of the coordinate x.

In terms of the short-ranged correlation functions and long-ranged potential parts, the OZ equations in wavenumber space can be written as the set of coupled algebraic equations

$$[\delta_{ik}-\chi_k\tilde{c}_{ik}^{(s)}+\chi_k\tilde{u}_{ik}^{(l)}]\tilde{\gamma}_{kj}^{(s)}=-\tilde{u}_{ij}^{(l)}-\chi_k\tilde{u}_{ik}^{(l)}\tilde{c}_{kj}^{(s)}+\chi_k\tilde{c}_{ik}^{(s)}\tilde{c}_{kj}^{(s)} \tag{12}$$

with Kronecker-delta δ_{ij}. The HNC closure in terms of the short-ranged correlation functions and the hard-core diameters is

$$c_{ij}^{(s)}(x)=\Theta(x-\sigma_{ij}n^{1/d})\exp\{\gamma_{ij}^{(s)}(x)\}-\gamma_{ij}^{(s)}(x)-1, \tag{13}$$

with unit step function $\Theta(x)$.

The Fourier transform of the Coulombic part $u_{ij}^{(l)}(x)$ of the potential is[60]

$$\tilde{u}_{ij}^{(l)}(y)=\frac{\Gamma_{ij}A(d)}{y^2}, \tag{14}$$

where $A(d)=2\pi^{d/2}/\Gamma(d/2)$ denotes the surface of the d-dimensional unit hypersphere.

We solve the closed set of eqs. (12)–(14) by the numeric methods described in the following two sections. Our results are presented in form of the partial rdf's $g_{ij}(x)$, and partial static structure factors, $S_{ij}(y)=\delta_{ij}+\sqrt{\chi_i\chi_j}\tilde{h}_{ij}(y)$[11,14]

Numerical algorithm

In order to solve the set of eqs. (12)–(14), we use a generalized version of the numerically robust, quickly convergent solution method introduced by Ng in the appendix of Ref. 56. The method shares great similarities with the direct inversion of iterative subspace (DIIS) method developed by Pulay,[61,62] which is commonly used in the solution of quantum mechanical (Hartree-Fock) density functional problems (see Ref. 63 for a detailed analysis of the DIIS method). The DIIS method has been applied also to density functional theory of hard spheres,[64] and reference interaction site model HNC equations of liquid water.[65]

In conformity with Ng's notation, we formulate a fixed point problem

$$\boldsymbol{A}\cdot\mathbf{c}^{(s)}(x)\stackrel{!}{=}\mathbf{c}^{(s)}(x), \tag{15}$$

to be fulfilled by the exact solutions $\mathbf{c}^{(s)}(x)$ of eqs. (12)–(14), for arbitrary values of the coordinate x. Equation (15) contains

the $m\times m$ function array $\mathbf{c}^{(s)}(x)$ with elements $c_{ij}^{(s)}(x)$, and the nonlinear fourth-rank operator $\boldsymbol{A}$, that depends on all pair potentials $u_{ij}(x)$.

We solve eq. (15) numerically by executing two nested instruction loops with iteration indices $n_1 \in \{\mathbb{N} \cap [0, n_1^{\max}]\}$ and $n_2 \in \mathbb{N}$, such that $\lim_{n_2\to\infty} \mathbf{c}^{(s)}_{\{n_1^{\max},n_2\}}(x)=\mathbf{c}^{(s)}(x)$, provided that the iteration with respect to index n_2 converges. To avoid confusion with other kinds of indices or with particle number densities in the following, n_1 and n_2 are exclusively used to label entire operators, matrices or vectors, and are never used in indexing scalars. Both n_1 and n_2 are always enclosed in curly brackets when used as an index, whereas other lower indices, like the species indices $i, j, \ldots$ stand always without brackets. For instance, $\mathbf{c}^{(s)}_{\{n_1,n_2\}}(x)$ is the $m\times m$ array of intermediate solutions for the short-ranged parts of partial direct correlation functions at iteration stage characterized by n_1 and n_2, and the element of that array with particle-species indices i and j is the function $(\mathbf{c}^{(s)}_{\{n_1,n_2\}})_{ij}(x)$.

In the outer loop with index n_1, the elements of an $m\times m$ matrix $\boldsymbol{\Gamma}_{\{n_1\}}$ of coupling parameters and an m-dimensional vector $\boldsymbol{\phi}_{\{n_1\}}$ of hypervolume fractions are both ramped up from initial values $(\boldsymbol{\Gamma}_{\{0\}})_{ij}$ and $(\boldsymbol{\phi}_{\{0\}})_i$ of small magnitude, to their final values $(\boldsymbol{\Gamma}_{\{n_1^{\max}\}})_{ij}=\Gamma_{ij}$ and $(\boldsymbol{\phi}_{\{n_1^{\max}\}})_i=\varphi_i$, characterizing the pair-potentials to be solved for through eqs. (1–4). We use the rules

$$\boldsymbol{\Gamma}_{\{n_1\}}=\varepsilon(n_1)\boldsymbol{\Gamma}_{\{n_1^{\max}\}} \tag{16}$$

and

$$\boldsymbol{\phi}_{\{n_1\}}=[\varepsilon(n_1)]^{1/10}\boldsymbol{\phi}_{\{n_1^{\max}\}} \tag{17}$$

for potential ramp-up, where a near-optimal convergence rate, combined with good numerical stability of the outer loop iteration is achieved by a convergence-adaptive scaling parameter $0 < \varepsilon \leq 1$, which increases monotonically as a function of n_1. After each outer iteration, the growth rate of $\varepsilon(n_1)$ is increased if the previous inner loop took less than a certain threshold of iterations to converge, and decreased in the opposite case.

Our experience shows that numerical stability of the algorithm benefits considerably from the superlinear form of eq. (17), characterized by the (empirically chosen) exponent 1/10. This can be rationalized by considering the contact value $u_{ij}(\sigma_{ij}n^{1/d}+)$ of the pair potential in eqs. (1–4), that is, the right-hand limit of $u(x)$ as x approaches the separation of particles with touching surfaces: The contact value decreases for increasing values of φ_i and φ_j, and increases for increasing Γ_{ij}. The potential at particle contact has great influence on the strength of the undulations in the pair-structure functions, which, in turn, influence numerical stability. Therefore, it is favorable to choose potential ramp-up rules like eqs. (16) and (17), where the φ_i are increased quicker than the Γ_{ij}.

That a potential ramp-up is necessary at all, is owed to critical dependence of the inner loop convergence on the quality of the inner loop seed $\mathbf{c}^{(s)}_{\{n_1,0\}}$. A good analytical estimate of $\mathbf{c}^{(s)}_{\{n_1,0\}}$ exists only for low magnitudes of all $(\boldsymbol{\Gamma}_{\{n_1\}})_{ij}$ and $(\boldsymbol{\phi}_{\{n_1\}})_i$. The inner iteration seeds used in our algorithm are given in eqs. (33–35), and rationalized in the surrounding text.

We proceed now with the discussion of the inner iteration loop, where n_1 is kept fixed. Operator $\boldsymbol{A}_{\{n_1\}}$ is defined by

$$\boldsymbol{A}_{\{n_1\}} \cdot \mathbf{c}^{(s)}_{\{n_1,n_2\}}(x)=\boldsymbol{\eta}^{(s)}_{\{n_1,n_2\}}(x), \tag{18}$$

as the operator that transforms the input functions arrays, $\mathbf{c}^{(s)}_{\{n_1,n_2\}}(x)$, for fixed indices n_1 and n_2, into the corresponding output functions arrays, $\boldsymbol{\eta}_{\{n_1,n_2\}}(x)$, the latter being defined further down the text of this subsection. Hence, $\boldsymbol{A}_{\{n_1^{\max}\}}=\boldsymbol{A}$, and eq. (15) is equivalent to

$$\lim_{n_2\to\infty} \boldsymbol{d}_{\{n_1^{\max},n_2\}}(x) \stackrel{!}{=} 0, \tag{19}$$

with function arrays $\boldsymbol{d}_{\{n_1,n_2\}}(x)$ defined by

$$\begin{aligned}\boldsymbol{d}_{\{n_1,n_2\}}(x)&=\boldsymbol{\eta}_{\{n_1,n_2\}}(x)-\mathbf{c}^{(s)}_{\{n_1,n_2\}}(x)\\&=(\boldsymbol{A}_{\{n_1\}}-1)\cdot\mathbf{c}^{(s)}_{\{n_1,n_2\}}(x).\end{aligned} \tag{20}$$

In our implementation, iteration in the inner loop is stopped at a finite, n_1-dependent value, $n_2^{\max}(n_1) > 1$, of the index n_2, once the convergence criterion

$$\frac{||\boldsymbol{d}_{\{n_1,n_2^{\max}(n_1)\}}(x)||}{||\boldsymbol{\eta}_{\{n_1,n_2^{\max}(n_1)\}}(x)||} < \mathrm{TOL}(n_1), \tag{21}$$

with a small tolerance $\mathrm{TOL}(n_1)$, as specified below, has been fulfilled. In eq. (21), the norm, $||\mathbf{f}(x)||$, of an $m\times m$ function array $\mathbf{f}(x)$, is defined as

$$||\mathbf{f}(x)||=\Big(\boldsymbol{f}(x),\boldsymbol{f}(x)\Big)^{1/2}, \tag{22}$$

and the bracket $(\boldsymbol{f},\boldsymbol{g})$ denotes the inner product

$$(\boldsymbol{f},\boldsymbol{g})=\int_{x_1}^{x_2}\boldsymbol{f}(x):\boldsymbol{g}(x)dx, \tag{23}$$

of two $m\times m$ function arrays $\boldsymbol{f}(x)$ and $\boldsymbol{g}(x)$ with elements $\boldsymbol{f}_{ij}(x)$ and $\boldsymbol{g}_{ij}(x)$, double dots indicating the contraction with respect to both particle species indices i and j. The interval $[x_1, x_2]$ should be chosen to contain the major structural features of the partial direct correlation functions. To obtain the results presented in this paper, we have used $x_1=\min\{0.5\sigma_i n^{1/d}, i=1\ldots m\}$, $x_2=30$, and values of TOL that decrease as a function of n_1, with $\mathrm{TOL}(0) < 10^{-4}$ and $\mathrm{TOL}(n_1^{\max}) < 10^{-12}$.

In our algorithm, $\boldsymbol{\eta}_{\{n_1,n_2\}}(x)$ is obtained from $\mathbf{c}^{(s)}_{\{n_1,n_2\}}(x)$ at fixed values of n_1 and n_2 by applying the following four steps:

Step 1. The function arrays $\mathbf{c}^{(s)}_{\{n_1,n_2\}}(x)$ are Fourier-transformed into $\tilde{\mathbf{c}}^{(s)}_{\{n_1,n_2\}}(y)$ by the fast transform method described in the following subsection, requiring logarithmically spaced grids in x- and y-space.

Step 2. The coupled OZ eq. (12) is solved to obtain $\tilde{\gamma}^{(s)}_{\{n_1,n_2\}}(y)$ from $\tilde{\mathbf{c}}^{(s)}_{\{n_1,n_2\}}(y)$.

Step 3. The fast inverse transform method on logarithmic grids is applied to compute the inverse Fourier transform, $\gamma^{(s)}_{\{n_1,n_2\}}(x)$, of the function array $\tilde{\gamma}^{(s)}_{\{n_1,n_2\}}(y)$.

Step 4. The elements of the function arrays $\boldsymbol{\eta}_{\{n_1,n_2\}}(x)$ are calculated as the left-hand-sides of eq. (13) (the HNC closure), where the elements of the function arrays $\gamma^{(s)}_{\{n_1,n_2\}}(x)$ from step 3 are entered to the right-hand-sides of eq. (13).

A straightforward way of selecting the input functions, $\mathbf{c}^{(s)}_{\{n_1,n_2+1\}}(x)$, for the next step of the inner loop, is the Picard-iteration scheme

$$\mathbf{c}^{(s)}_{\{n_1,n_2+1\}}(x)=\boldsymbol{\eta}_{\{n_1,n_2\}}(x). \tag{24}$$

This simple scheme, however, converges only for weak pair-potentials (small values of $|\Gamma_{ij}|$ and φ_i, in our case).

Numerical stability of the Picard-iteration scheme can be somewhat improved, at the cost of increasing computational effort, if a fixed mixing parameter $0<\alpha<1$ is introduced in eq. (24), which gives the alternative iteration rule

$$\mathbf{c}^{(s)}_{\{n_1,n_2+1\}}(x)=\alpha\boldsymbol{\eta}_{\{n_1,n_2\}}(x)+(1-\alpha)\mathbf{c}^{(s)}_{\{n_1,n_2\}}(x). \tag{25}$$

Fixed point iterations on basis of eqs. (24) or (25) have been applied in a number of integral equation studies,[23,27,33,39,40,66,67] where different strategies have been applied in computing the Fourier transforms, and various closure relations for the OZ-equations have been used, including the HNC closure. The mixing parameter α in eq. (25) has been empirically determined in most cases.

Despite being numerically more robust than the Picard iteration in eq. (24), the iteration scheme according to eq. (25) still fails to converge for large values of $|\Gamma_{ij}|$ or φ_i, especially if the number of components, m, is larger than one. We therefore use a generalized version of the fixed point iteration scheme proposed by Ng,[56] which has proven to be numerically much more stable and efficient. Ng's iteration scheme, generalized to m-component mixtures and arbitrary number, $M\geq 0$, of mixing coefficients, reads

$$\begin{aligned}\mathbf{c}^{(s)}_{\{n_1,n_2+1\}}(x)=&\left(1-\sum_{l=1}^{M}(\boldsymbol{\alpha}_{\{n_1,n_2\}})_l\right)\boldsymbol{\eta}_{\{n_1,n_2\}}(x)\\&+\sum_{l=1}^{M}(\boldsymbol{\alpha}_{\{n_1,n_2\}})_l\boldsymbol{\eta}_{\{n_1,n_2-l\}}(x).\end{aligned} \tag{26}$$

For $M=0$, eq. (26) reduces to the Picard iteration in eq. (24). At every step of the iteration, the M-dimensional mixing coefficient vector $\boldsymbol{\alpha}_{\{n_1,n_2\}}$ is determined as the solution of the set of linear equations

$$\Delta_{\{n_1,n_2\}}\cdot\boldsymbol{\alpha}_{\{n_1,n_2\}}=\boldsymbol{\delta}_{\{n_1,n_2\}}, \tag{27}$$

where the elements,

$$(\Delta_{\{n_1,n_2\}})_{lm}=(\mathbf{v}_{\{n_1,n_2,l\}},\mathbf{v}_{\{n_1,n_2,m\}}) \tag{28}$$

and

$$(\boldsymbol{\delta}_{\{n_1,n_2\}})_l=(\mathbf{d}_{\{n_1,n_2\}},\mathbf{v}_{\{n_1,n_2,l\}}), \tag{29}$$

of the $M\times M$ matrix $\Delta_{\{n_1,n_2\}}$ and the vector $\boldsymbol{\delta}_{\{n_1,n_2\}}$ are inner products involving the function arrays $\mathbf{d}_{\{n_1,n_2\}}$ and

$$\mathbf{v}_{\{n_1,n_2,l\}}=\mathbf{d}_{\{n_1,n_2\}}-\mathbf{d}_{\{n_1,n_2-l\}}. \tag{30}$$

Solving for $\boldsymbol{\alpha}_{\{n_1,n_2\}}$ in eqs. (27)–(30) is equivalent to solving the minimization problem

$$||\mathbf{d}_{\{n_1,n_2\}}-\sum_{l=1}^{M}(\boldsymbol{\alpha}_{\{n_1,n_2\}})_l\mathbf{v}_{\{n_1,n_2,l\}}||\stackrel{!}{=}\min, \tag{31}$$

with respect to $\boldsymbol{\alpha}_{\{n_1,n_2\}}$, and the minimization in expression (31) can be motivated by approximating $\mathbf{A}_{\{n_1\}}$ as a locally linear operator.[56,68]

It may be counterintuitive, but is worthwhile to note that one should not select $M=n_2$, that is, the maximum possible order at each inner loop iteration. Instead, numerical stability is increased if one chooses M to rise slower than possible, in our case as

$$M(n_2)=\begin{cases}\min\{n_2,M^{\max}\} & \text{for } n_2\leq 5,\\ \min\{2+\lfloor n_2/2\rfloor,M^{\max}\} & \text{for } n_2>5,\end{cases} \tag{32}$$

with $\lfloor a\rfloor$ denoting the largest integer number smaller than or equal to a, and $M^{\max}=20$, which results in swift convergence. Presumably, the reason for the increased numerical stability of the rule in eq. (32) as compared to the rule $M=n_2$, is that the low-quality intermediate solutions for small values of n_2 are always retained in the mixing rule in eq. (26) if $M=n_2$ is chosen, whereas they are dismissed, and thereby prevented from spoiling convergence at sufficiently high n_2, if M rises more slowly than n_2.

The iteration scheme defined by eqs. (26)–(30) fails to converge, if the seed of the inner loop iteration, $\mathbf{c}^{(s)}_{\{n_1,0\}}(x)$, is too different from the fixed point of operator $\mathbf{A}_{\{n_1\}}$. A good analytical estimate of an iteration seed exists only for sufficiently small coupling parameters and hypervolume fractions. In this regime, one may approximate the $c_{ij}(x)$ by their infinite dilution (number density $n\to 0$) limit $c_{ij}(x)\to f_{ij}(x)=\exp\{-u_{ij}(x)\}-1$, where the $f_{ij}(x)$ are the Mayer functions.[11,67] This results in a seed

$$\mathbf{c}^{(s)}_{\{0,0\}}(x)=\exp[-\mathbf{u}_{\{0\}}(x)]-1+\mathbf{u}_{\{0\}}(x) \tag{33}$$

for $n_1=n_2=0$, where $\mathbf{u}_{\{n_1\}}(x)$ denotes an array of pair-potentials $(\mathbf{u}_{\{n_1\}})_{ij}(x)$ between particles of species i and j, obtained from inserting the potential parameters $(\boldsymbol{\Gamma}_{\{n_1\}})_{ij}$ and $(\boldsymbol{\phi}_{\{n_1\}})_i$ into eqs. (1–4).

To access HNC solutions at higher $|\Gamma_{ij}|$ and φ_i, we construct the seeds for $n_1>0$ from the converged solutions of inner iterations corresponding to smaller values of n_1. For $n_1=1$, we choose

$$\mathbf{c}^{(s)}_{\{1,0\}}(x)=\boldsymbol{\eta}_{\{0,n_2^{\max}(0)\}}(x), \tag{34}$$

which is a Picard-iteration step in the outer loop. For $n_1 > 1$, we use the seed

$$\begin{aligned}\mathbf{c}^{(s)}_{\{n_1,0\}}(x)&=s^{(1)}\boldsymbol{\eta}_{\{n_1-1,n_2^{\max}(n_1-1)\}}(x),\\ &+s^{(2)}\boldsymbol{\eta}_{\{n_1-2,n_2^{\max}(n_1-2)\}}(x),\end{aligned} \tag{35}$$

with coefficients

$$s^{(1)}=\frac{\varepsilon(n_1)-\varepsilon(n_1-2)}{\varepsilon(n_1-1)-\varepsilon(n_1-2)} \tag{36}$$

and

$$s^{(2)}=\frac{\varepsilon(n_1)-\varepsilon(n_1-1)}{\varepsilon(n_1-1)-\varepsilon(n_1-2)}, \tag{37}$$

that extrapolate linearly on basis of the previous two converged inner iteration solutions. While the linear extrapolation in eq. (35) is crucial for numerical stability at strong particle correlations, generalizing to quadratic and higher orders of polynomial extrapolation for $n_1 > 2$ seems to have a weakening effect on numerical stability.

Variations of Ng's fixed point iteration method have been successfully applied in various liquid integral equation studies.[19,22,56,65,69–74] General performance figures of the algorithm in eqs. (26–37) are difficult to formulate, as its efficiency depends on the number of particle species and spatial dimensions, and, most importantly, on the pair-potential parameters. All individual HNC solutions presented in this article took few minutes or less to be computed on an inexpensive personal computer.

Note that the fixed point iteration scheme in eqs. (26–37) is merely one among a wide variety of solution methods that have been developed. Part of the alternative solution methods have been reported to show superior numerical efficiency, at the cost of a more complicated implementation. Along with Ng's algorithm, Newton-Raphson-like fixed-point iteration schemes, first introduced by Gillan,[75] Labík et al.,[76] and Zerah,[77] are routinely used in integral equation studies of liquids with strong pair-correlations.[17,20,21,78–86] For an elaborate comparison of Ng's and Zerah's methods, including a formulation of the latter method for liquid mixtures, we refer to appendix A of Ref. 68. Furthermore, highly elaborate Newton-GMRES (Krylov subspace) algorithms have been applied,[87] and have been combined with multigrid techniques.[88] Yet another alternative approach is the vector extrapolation method.[89] For the sake of simplicity, in this study we do not use the methods laid out in Refs. 75–77,87–89. In future studies, however, use of such elaborate fixed point solution methods, in combination with the Fourier transform method described in the following subsection, might give access to liquid integral equation solutions of the PM for even larger ion-size and charge asymmetries than accomplished in this work.

Fourier transform on logarithmic grids

In this subsection, we present our numerical method of choice to approximate the forward- and backward Fourier transforms in eqs. (6) and (7), for functions $f(x)$ and $\tilde{f}(y)$ that are sampled on finite computational grids. The method used here has been devised in essence by Talman, [36] and constitutes a sophisticated version of the so-called quasi-fast Hankel transform method of Siegman.[35] It is based on the use of logarithmic variables, that is, computational grids of the form

$$x_n=x_0\exp\{nL/N\},\qquad y_n=y_0\exp\{nL/N\}, \tag{38}$$

with grid index n in the range $-\lfloor N/2\rfloor \le n \le \lfloor N/2\rfloor$, and $L, N > 0$. The use of logarithmic grids has been motivated by the work of Gardner et al.[34] As demonstrated in Ref. 35, sampling on logarithmic grids allows to rewrite eqs. (6) and (7) as discrete circular correlations, each of which can be treated by applying two subsequent FFTs. For a complete, and particularly clear-cut documentation, we refer to the work of Hamilton, [37,38] where the method has been named FFTLog. As we have closely followed Refs. 37,38 in our implementation of the FFTLog transform, we refrain from repeating all details here, and list only the essential expressions instead.

Adapting to the notation of Refs. 37,38, we define the primed sum symbol $\sum'$ through

$$\sum_n{}' x_n=\sum_{n=-\lfloor N/2\rfloor}^{\lfloor N/2\rfloor} w_n x_n, \tag{39}$$

with weights $w_n=1$ for all n, except for $w_{-N/2}=w_{N/2}=1/2$ if N is even.

In a preprocess, preceding the many FFTLog transforms occurring in the fixed point iteration described in the previous subsection, lookup tables of the grid-specific coefficients

$$u_n=\left(\frac{2}{x_0y_0}\right)^{2\pi in/L}\Gamma\left[\frac{d}{4}+\frac{\pi in}{L}\right]/\Gamma\left[\frac{d}{4}-\frac{\pi in}{L}\right] \tag{40}$$

are computed. As pointed out in Refs. 36,39, numerical evaluation of eq. (40) for large arguments of the Gamma functions is considerably simplified by noticing that $|\Gamma(x+iy)/\Gamma(x-iy)|=1$ for $x, y \in \mathbb{R}$. The remaining problem of determining the complex phases of the Gamma functions in eq. (40) is conveniently solved in resorting to Ref. 90. An alternative way to determine the complex phases has been devised in Ref. 39, where the problem was tackled using recurrence relations of the Gamma function.

The forward FFTLog transform from the space of dimensionless distances x to the space of dimensionless wavenumbers y can be evaluated as[37,38]

$$\tilde{f}(y_n)=\left(\frac{2\pi}{y_n}\right)^{d/2}\sum_m{}' c_m u_m \exp\{\frac{-2\pi imn}{N}\}, \tag{41a}$$

$$c_m=\frac{1}{N}\sum_n{}' f(x_n)x_n^{d/2}\exp\{\frac{-2\pi imn}{N}\}, \tag{41b}$$

and the inverse transform (from y- to x-space) reads[37,38]

$$f(x_n) = x_n^{-d/2} \sum_m{}' \frac{\tilde{c}_m}{u_m^*} \exp\left\{\frac{-2\pi imn}{N}\right\}, \quad (42a)$$

$$\tilde{c}_m = \frac{1}{N} \sum_n{}' \tilde{f}(y_n) \left(\frac{y_n}{2\pi}\right)^{d/2} \exp\left\{\frac{-2\pi imn}{N}\right\}, \quad (42b)$$

with the star denoting the complex conjugate. Being nothing else but discrete, one-dimensional Fourier transforms, all four eqs. (41a–42b) can be solved by numerically efficient FFT algorithms, which are available in a great variety of implementations. Here, we use a mixed-radix FFT routine,[90] imposing no constraints on the number of grid points $2\lfloor N/2 \rfloor + 1$.

For validity of eqs. (41b) and (42b), it is necessary to fulfill the constraint $u_{-\lfloor N/2 \rfloor} = u_{\lfloor N/2 \rfloor}$ in choosing the parameters x_0, y_0, N, and L of the grids in eq. (38). Fulfilling this constraint is equivalent to

$$\frac{N \ln(x_0 y_0)}{L} = \frac{1}{\pi} \mathrm{Arg}\left[2^{\pi i N/L} \frac{\Gamma(d/4 + \pi i N/(2L))}{\Gamma(d/4 - \pi i N/(2L))}\right] + z, \quad (43)$$

with an arbitrary integer number z, and Arg[c] denoting the phase of complex number c. In Refs. 37,38, the criterion in eq. (43) has been named the low-ringing condition. In all calculations with results presented here, we have chosen $x_0 = 1$, and $x_0 y_0 \approx 1$, while fulfilling eq. (43).

An important virtue of the FFTLog transform in eqs. (40–42b) is its computational efficiency for arbitrary dimensions d. Choosing the number of grid points as an integer power of 2 results in optimal performance of the transforms in eqs. (41a–42b), each requiring $\mathcal{O}(N \log_2 N)$ arithmetic operations in that case. We note here that an alternative, numerically efficient method of calculating d-dimensional Fourier-Bessel transforms of the kind of eqs. (6) and (7) has been used in Refs. 91–94. In this alternative approach, which does not require logarithmic grids, the Fourier-Bessel transforms are replaced by a sequence of so-called hat transforms and FFTs.

For even d, in particular for $d = 2$, numerically less efficient methods for computing the transforms in eqs. (6) and (7) have been reported,[95–97] each of which requires $\mathcal{O}(N^2)$ arithmetic operations. Such numerically suboptimal $\mathcal{O}(N^2)$ transforms have been applied in various liquid integral equation studies.[23,67,98]

For $d = 3$ (odd number of dimensions, in general), using the transform in eqs. (39)–(43) is not obvious as the standard FFT can be directly applied to functions sampled on grids with uniform spacing. Uniformly spaced grids, however, are not ideally suited for sampling the correlation functions of highly asymmetric PM fluids. Ion size and charge-ratios of the order of 1:1000 in typical colloidal suspensions render it necessary to simultaneously resolve length scales that differ by a factor of more than 1000, which requires huge numbers of grid points in uniformly spaced grids. For instance, in Ref. 27, $2^{18} = 262,144$ points had to be used to sample correlation functions for ion diameter asymmetry of 1:80 and charge asymmetries up to 1:450 (at nonzero macroion number density), resembling only rather small macroions. Logarithmic grids, conversely, are ideally suited to capture the different length scales in (asymmetric) charged sphere systems, as it has been first pointed out by Rossky and Friedman.[33] Logarithmic grids have later been used in $d = 3$ liquid integral equation studies[41–43] but, to our knowledge, no liquid integral equation study has been conducted so far, where the advantages of the transform in eqs. (39)–(43) have been exploited in solving pair correlations of an extremely asymmetric PM. Our results presented here, for ion charge- and size-ratios both simultaneously as high as 1:1000, have been obtained using no more than $2^{13} = 8192$ grid points.

In addition to ionic mixtures, suspensions of electrically neutral, nonoverlapping hard (hyper)spheres, for which $\Gamma_{ij} = 0$ in eq. (4), are a salient testing ground for the applicability of the numerical algorithm presented here. The rdf's of hard sphere suspensions exhibit narrowly spaced undulations in the rdf's $g_{ij}(x)$, with a periodicity that is approximately equal to the dimensionless hard-core diameter $\sigma_{ij} n^{1/d}$.[99] For logarithmic grids with exponentially increasing spacing of the gridpoints, one might therefore expect severe undersampling of hard-sphere rdf's for large values of x. This kind of undersampling, however, is of negligible influence, since the hard-sphere total correlation functions $h_{ij}(x)$ decay very steeply to values that are in the range of the numerical resolution of common digital computers. Using representative values for $d = 3$ hard sphere suspensions with nonadditive hard-core diameters, taken from Ref. 99, we have checked that our algorithm converges reliably, even for nonadditive hard sphere mixtures close to the critical fluid–fluid demixing point.

MD simulations

In this article, we present MD simulation data for fluids in $d = 3$ spatial dimensions only. We have simulated globally electroneutral systems with three or four different ion species in a cubic box of edge length B with periodic boundary conditions in all three Cartesian directions. The MD simulation method used here is the same as in Refs. 8,100. In order to handle the long-ranged Coulomb interactions, we use the Lekner summation method,[101–103] which takes the real-space particle coordinates as its only input. An alternative way to handle the Coulomb interactions is the Ewald summation method,[104] where the Coulomb interactions are split into two quickly convergent sums in real space and reciprocal (wavenumber) space. Both methods are of comparable numerical expense, and have been successfully applied to colloidal systems in $d = 3$ dimensions. For a comprehensive review of the computation of long-ranged interactions, including the Ewald and Lekner summation methods, we refer to Ref. 105.

All parameters for the simulations presented here are listed in Table 1, with N_i denoting the total number of particles of species i in the simulation box, such that $n_i = N_i/B^3$. All simulations are for a Bjerrum length of $L_B = 0.701$ nm, corresponding to water at room temperature. A representative snapshot of particle positions for the four-component system (rightmost column of Table 1) is shown in Figure 1.

On average, 1 week of execution time on a 64 bit computer cluster is enough to get fairly good statistics for the

Table 1. Parameters for the $d = 3$ MD simulations of the present study.

Results in	Ternary Fig. 3	Quaternary Fig. 4
N_1	48	24
N_2	4080	24
N_3	6280–28080	1900
N_4	-.-	13680
σ_1	150 nm	122 nm
σ_2	0.60 nm	68 nm
σ_3	0.60 nm	0.61 nm
σ_4	-.-	0.61 nm
Z_1	25–500	380
Z_2	1	190
Z_3	−1	1
Z_4	-.-	−1
B/σ_1	7.951	7.566

The N_i are the numbers of particles of species i in the cubic box of edge length B.

macroion–macroion and the macroion–microion correlation functions, for the systems consisting of up to 32,208 charged particles. Achieving comparably good microion–microion statistics would require even much longer execution times, due to the small relevant microion–microion scattering cross section, the overall rather small number density of microions, and the short binning length that would be required to extract sensible microion–microion radial distribution functions from the raw MD data. Therefore, we restrict ourselves here to comparisons of macroion–macroion and macroion–microion pair correlations obtained from MD simulations and the HNC scheme.

Results

Thermodynamical properties and pair-correlations in one to six dimensions

As a first result, the HNC solutions computed in our numerical algorithm are in agreement with the d-dimensional local electroneutrality (LEN) conditions

$$\mathrm{sgn}(Z_i)\sqrt{|\Gamma_{ii}|} \stackrel{!}{=} -\lim_{x\to\infty} A(d)\int_0^x dx'\tau_i(x')x'^{d-1}, \qquad (44)$$

where $\tau_i(x)$, defined as

$$\tau_i(x) = \chi_i \mathrm{sgn}(Z_iZ_j)\sqrt{|\Gamma_{ij}|}g_{ij}(x) \qquad (45)$$

is the isotropic charge density around a test particle of species i. In eqs. (44) and (45), $\mathrm{sgn}(x)$ is the sign function. The LEN condition states that the total charge of ions around a test particle cancels out with the test particle's charge. If a computational grid is chosen that extends to a very large outer radius $x_{\lfloor N/2 \rfloor}$, we find the LEN condition in eq. (44) violated at large x, where the functions $c_{ij}^{(s)}(x)$ and $\gamma_{ij}^{(s)}(x)$ assume values too small to be resolved at machine precision. However, if taking the $x \to \infty$ limit in eq. (44) is replaced by insertion of an intermediately large value of $x \approx 100$, where the oscillations in all $g_{ij}(x)$ have essentially died out, we find eqs. (44) fulfilled to within good accuracy.

In the special case of $m = 1$, our algorithm allows to compute pair-correlations of the OCP in arbitrary dimensions, as illustrated in Figure 2. Note here the good quality of the HNC solutions at small wavenumbers, where the vanishing compressibility of the OCP, with $\lim_{y\to 0} S_{11}(y)=0$, is well described. The magnitude of the undulations in the $S_{11}(y)$ and $g_{11}(x)$ plotted in Figure 2 is a nonmonotonic function of the dimension d, with maximal undulations occurring for $d = 3$.

In Figures 3 and 4, we compare the HNC rdf's $g_{ij}(r)$ for three- and four-component PMs in $d = 3$ to the results of our MD simulations. Overall good agreement is observed between the HNC and MD results, the most prominent discrepancy being an underestimation (of up to about 20%) of the principal peak height in the HNC macroion–macroion rdf's, occurring at strong macroion correlations. Underestimation of the principal peak heights in the macroion–macroion pair-correlation functions is a known shortcoming of the HNC,[11,106,107] which can be tackled by choosing an alternative, thermodynamically partially self-consistent integral equation scheme. [13–16] An alternative method to improve the accuracy of the HNC consists in using a tailored Ansatz[56,98] for the bridge function[11] at high coupling, which is neglected altogether in the HNC.

In Figure 5, we display all HNC partial rdf's and static structure factors of three-component, globally electroneutral PMs in all integer dimensions d from 2 to 6. The dimensionless pair-potential parameters are the same for all systems in the figure, with coupling constants $\Gamma_{22}=\Gamma_{33}=-\Gamma_{23}=0.01$, $\Gamma_{13}=-\Gamma_{12}=25$, and $\Gamma_{11}=625$, corresponding, for $d = 3$, to $Z_1=250$,

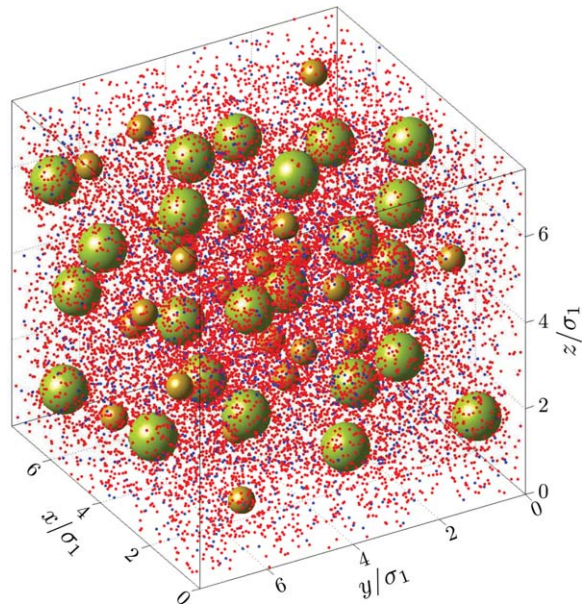

Figure 1. A representative snapshot of particle positions from our MD simulations of a four-component, three dimensional PM (right column of Table 1, with rdf's shown in Fig. 4). The full simulation box is shown. Two macroion species (green and bronze) of different diameters and charge numbers are contained. Sizes of coions (blue) and counterions (red) are exaggerated, to render the microions visible.

$Z_2=-1$, $Z_3=1$, and $L_Bn^{1/3}=0.1$. The hypervolume fraction of species 1 is $\varphi_1=0.01$ for all systems in Figure 5, and $n_3=n_1\sqrt{\Gamma_{11}}$, which means that there is one salt coion per macroion-surface released counterion. A rather small ratio of macroion- to microion diameters, $\sigma_1/\sigma_2=\sigma_1/\sigma_3=5$, has been chosen for the systems in Figure 5 since, for larger size asymmetry, the solution in higher dimensions such as $d = 6$ becomes numerically very slowly convergent or divergent. Note that Figure 5 features panels with double logarithmic as well as logarithmic-linear axes, and that the axes ranges vary from panel to panel, to exhibit simultaneously the details of the various plotted functions.

In Figure 5, the $g_{ij}(x)$ and $S_{ij}(y)$ with the most pronounced oscillations around the asymptotic value one are for $d = 2$. For rising dimension and fixed dimensionless potential parameters, particle packing becomes less efficient and the decay of the Coulomb potentials becomes steeper. Therefore, the undulations in the pair-correlation functions get reduced for rising d until, for $d = 6$, the undulations have almost completely died out.

Application to the colloidal domain

Figure 6 features all HNC $g_{ij}(x)$ and $S_{ij}(y)$ for a $d = 3$, ternary PM that resembles a realistic suspension of colloidal particles in aqueous ($L_B=0.70$ nm) electrolyte with a low concentration of dissociated NaCl. The diameter of the macroions is taken to be $\sigma_1=1\,\mu$m, corresponding to rather large colloidal particles, while the diameters $\sigma_2=0.756$ nm and $\sigma_3=0.922$ nm correspond to hydrated Na^+ and Cl^- ions, respectively. Here, we have chosen the concentration of Cl^- coions (species 3) as $n_3=n_1|Z_1|$, so that the suspension contains one coion per colloid-surface released counterion, and overall about twice as many counterions as coions, $n_2 \approx 2n_3$. With the assumed macroion charge $Z_1=-750$, which is a realistic bare charge for a micron-sized colloidal sphere, this gives a coion concentration of $n_3=0.71\,\mu$M. This corresponds to an almost deionized aqueous solvent with a little amount of dissociated salt only (c.f., the number concentration, $n=0.1\,\mu$M, of the water self-dissociation products H_3O^+ and OH^- at neutral pH-value, which is a lower bound for the coion concentration).

Effective colloidal interactions

As a dimensionless effective pair potential between particles of the same species a in an m-component fluid mixture, one can define[79]

$$u_{aa}^{\mathrm{eff}}(x)=h_{aa}(x)-c_{aa}^{\mathrm{eff}}(x)-\ln\left[g_{aa}(x)\right], \tag{46}$$

where $c_{aa}^{\mathrm{eff}}(x)$ is an effective direct correlation function between particles of species a. The Fourier transform of the latter is

$$\tilde{c}_{aa}^{\mathrm{eff}}(y)=\frac{\tilde{h}_{aa}(y)}{1+\chi_a\tilde{h}_{aa}(y)}, \tag{47}$$

with the total correlation function $\tilde{h}_{aa}(y)=\tilde{\gamma}_{aa}(y)+\tilde{c}_{aa}(y)=\tilde{\gamma}_{aa}^{(s)}(y)+\tilde{c}_{aa}^{(s)}(y)$ taken from the solution of the coupled m-component set of eqs. (12–14). Equations (46) and (47) constitute an inversion of the HNC for species a only, meaning that a one-component fluid of particles with pair-potential $u_{aa}^{\mathrm{eff}}(x)$, solved within the HNC approximation, shows exactly the same pair-correlation functions as component a of the m-component mixture.

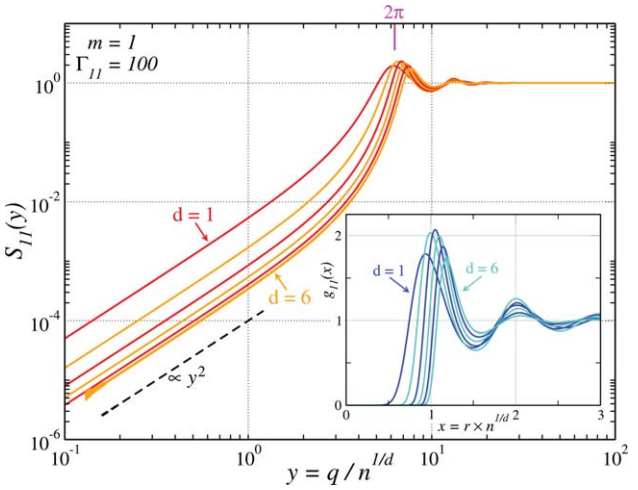

Figure 2. OCP ($m = 1$) static structure factors, $S_{11}(y)$, and rdf's, $g_{11}(x)$, for coupling parameter $\Gamma_{11}=100$ and hypervolume fraction $\varphi_1=10^{-3}$. The value of φ_1 is in every case small enough to ensure a practically vanishing rdf contact value, $g_{11}(x=\sigma_{11}n^{1/d}) \approx 0$. Correlation functions for systems in all integer dimensions from $d = 1$ to $d = 6$ are plotted. Principal peak positions of $S_{11}(y)$ and $g_{11}(x)$ shift from left to right as d increases.

Consider now a three-dimensional, ternary ionic liquid mixture of macroionic spheres (species a) with diameter σ_a and charge number Z_a, monovalent counterions, and monovalent coions. In this case, the repulsive part of the dimensionless Derjaguin-Landau-Verwey-Overbeek (DLVO) effective pair potential between two macroions at a nonoverlap center-to-center distance $x > \sigma_a n^{1/3}$ can be written as[108]

$$u_{aa}^{\mathrm{DLVO}}(x)=\Gamma_{aa}\,\frac{e^{k\sigma_a n^{1/3}}}{\left(1+\frac{k\sigma_a n^{1/3}}{2}\right)^2}\,\frac{e^{-kx}}{x}, \tag{48}$$

with $\Gamma_{aa}=L_Bn^{1/3}Z_a^2$, as defined further up this text. Equation (48) involves the dimensionless DLVO screening parameter k, which is given by

$$k^2=4\pi L_Bn^{1/3}(\chi_a|Z_a|+2\chi_{\mathrm{coion}}) \tag{49}$$

with χ_{coion} denoting the mole fraction of coions. The DLVO potential in eq. (48) is valid for two macroions in a bath of microions whose distribution can be treated in the Debye-Hückel approximation. It is thus valid only at low-macroion concentration, and for $L_BZ_a/\sigma_a \lesssim 1$, that is, for ionic pair interactions that do not considerably exceed the thermal energy. Under conditions where $L_BZ_a/\sigma_a > 1$, the potential in eq. (48) is nevertheless a good approximation to the effective macroion pair-potential at sufficiently large particle separation, provided that the charge number Z_a, entering via Γ_{aa} and eq. (49), is replaced by an effective charge number $Z_a^{\mathrm{eff}} < Z_a$.[44,46,49,109–117] The

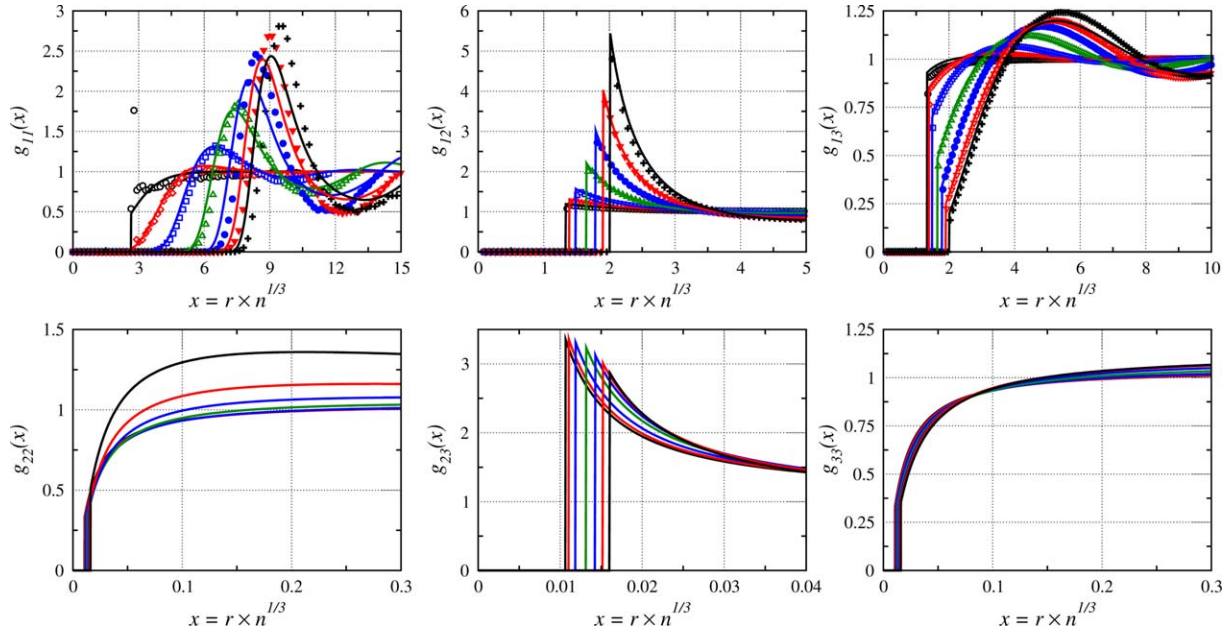

Figure 3. HNC (solid curves) results for all partial rdf's of three-dimensional, three-component, globally electroneutral PMs. Macroion–macroion and macroion–microion rdf's are compared with MD simulation results (symbols) in the upper row of panels. Each panel corresponds to a fixed particle-species pairing, as indicated on the vertical axes labels. Common system parameters are $\sigma_1 = 150$ nm, $\sigma_2 = \sigma_3 = \sigma_1/250 = 0.6$ nm, $L_B = 0.701$ nm, $\varphi_1 = 0.05$, $n_3 = 4\,\mu$M $Z_2 = -1$, $Z_3 = 1$. The macroion charge number, Z_1, has been varied, assuming the values $Z_1 = 25$ (open black circles, black lines), $Z_1 = 50$ (open red diamonds, red lines), $Z_1 = 100$ (open blue squares, blue lines), $Z_1 = 200$ (open green upwards triangles, green lines), $Z_1 = 300$ (filled blue circles, blue lines), $Z_1 = 400$ (filled red downward triangles, red lines), and $Z_1 = 500$ (black crosses, black lines). [Color figure can be viewed in the online issue, which is available at wileyonlinelibrary.com.]

effective charge $Z_a^{\text{eff}} e$ has to be regarded as the net charge of a colloid dressed with closely associated counterions.

While theories for the saturation value, $Z_a^{\text{eff}}(Z_a \to \infty)$, of the effective charge number are available,[112,113,118] calculation of the nonsaturated effective charge in a PM, in its full dependence on the concentrations and charges of all ionic species, remains a challenging task. Two approximate theories must be mentioned at this point, which are being extensively used to calculate colloidal effective charges. The first approach is commonly referred to as the CM and has been introduced by

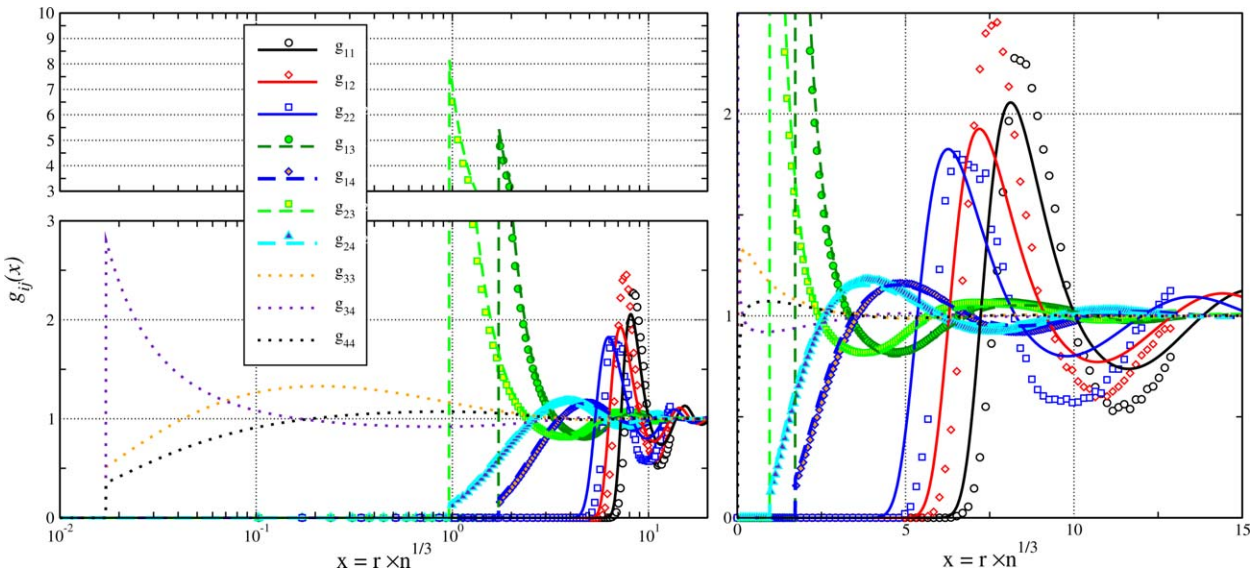

Figure 4. HNC (solid, dashed, and dotted curves) results for all partial rdf's of a three-dimensional, four-component, globally electroneutral PM. Macroion–macroion and macroion–microion rdf's are compared with MD simulation results (symbols). Species 1 and 2 are macroions with charges of equal sign, where species 1 is more strongly charged and possesses a larger hard-core diameter than species 2. Species 3 are the counterions, which are of equal size, but opposite charge, as the coions of species 4. System parameters are $\sigma_1 = 122$ nm, $\sigma_2 = 68$ nm, $\sigma_3 = \sigma_4 = \sigma_1/200 = 0.61$ nm, $L_B = 0.701$ nm, $\varphi = \sum \varphi_i = 0.034$, $n_1 = n_2$, $n_4 = 4\,\mu$M $Z_1 = 380$, $Z_2 = 190$, $Z_3 = -1$, $Z_4 = 1$. The left two panels are in logarithmic-linear scale, and the right panel exposes the details of the macroion–macroion rdf's on a doubly linear scale. [Color figure can be viewed in the online issue, which is available at wileyonlinelibrary.com.]

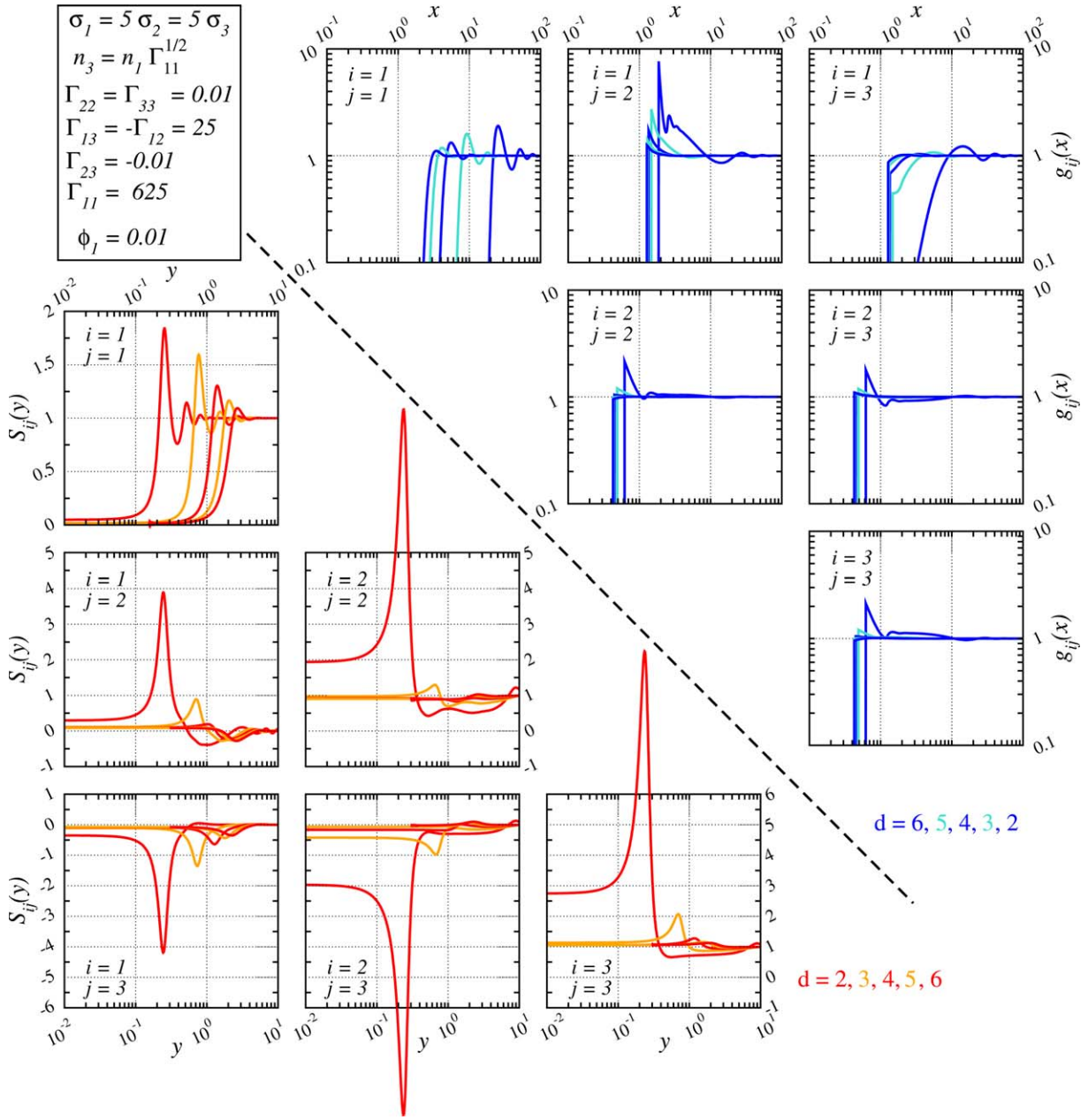

Figure 5. HNC partial rdf's $g_{ij}(x)$ (dark and light blue) and partial static structure factors $S_{ij}(y)$ (red and orange) of three-component, globally electroneutral PMs in d=2, 3, 4, 5, and 6 spatial dimensions, with equal dimensionless pair-potential parameters as indicated in the box in the upper left corner. The undulations in the functions are strongest for $d = 2$, and decay with rising dimension d. All rdf's are plotted in double-logarithmic scales of equal horizontal and vertical axes ranges. The horizontal y-axis ranges are equal in all structure factor plots, and the vertical $S_{ij}(y)$-axis ranges are $[0, 2]$ for i=j=1, $[-1, 6]$ for $j = 2$ and for i=j=3, and $[-6,1]$ for j=3 $\neq i$. The peak positions of the three $d = 2$ partial static structure factors that exceed their panel's vertical axis ranges are $S_{22}(y{=}0.237){=}9.0$, $S_{23}(y{=}0.237){=}-9.5$, and $S_{33}(y{=}0.236){=}10.7$. [Color figure can be viewed in the online issue, which is available at wileyonlinelibrary.com.]

Alexander et al. [44] In this approach, the coupled Poisson and Boltzmann (PB) equations for the microion distribution are numerically solved in a spherical cell reminiscent to the Wigner-Seitz cell of a crystal, with the diameter of the cell chosen equal to the colloidal mean geometric distance $\sim n_a^{-1/3}$. The CM allows to compute approximate values for Z_a^{eff}, and its dependence on Z_a and the concentration of all ion species. However, macroion correlation effects are represented only in a minimalistic fashion in the CM, by a contraction of the cell at rising particle concentration.

A second, alternative mean-field like approach to determine Z_a^{eff} is the RJM by Trizac and Levin.[46] In the RJM, the macroion charges entering the PB equation are approximated as a homogeneous background charge density (the "jellium") of a magnitude $-n_a Z_a^{\mathrm{eff}} e$, which has to be determined self-consistently. Later works comprise modifications of the RJM, where macroion correlations are accounted for in a minimalistic model for the macroion–macroion rdf with a density-dependent correlation hole,[9,47] or via the Rogers-Young integral equation scheme,[106] solved self-consistently in combination with the PB equation.[49]

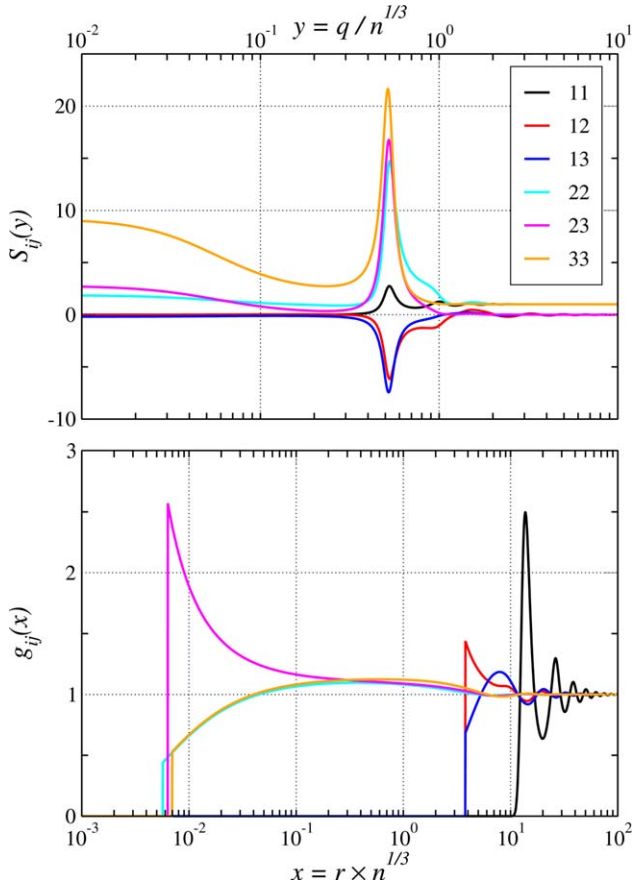

Figure 6. All HNC partial static structure factors (top) and rdf's (bottom) for a three-dimensional, three-component PM of micrometer-sized colloids in aqueous NaCl electrolyte. Particle-species indices corresponding to each curve are given in the legend. Parameters: $\sigma_1 = 1000$ nm, $\sigma_2 = 0.756$ nm (hydrated Na^+), $\sigma_3 = 0.922$ nm (hydrated Cl^-), $Z_1 = -750$, $Z_2 = 1$, $Z_3 = -1$, $\varphi_1 = 0.1$, $L_B = 0.70$ nm, $n_3 = n_1|Z_1|$ (one coion per surface-released counterion). [Color figure can be viewed in the online issue, which is available at wileyonlinelibrary.com.]

In Ref. 50, the RJM has been revisited and an efficient solution method for the self-consistent solution has been proposed, where the colloidal bare charge is avoided as an input parameter. The same method has been extended to suspensions containing macroions of different size and charge.[51] The CM, the RJM, and related schemes where the PB equation has been solved for particle configuration obtained from Monte Carlo simulation, are routinely being used in determining the microstructure in suspensions of highly charged colloidal particles.[48]

Here, we determine the effective charge by replacing Z_a with $Z_a^{\rm eff}$ in eqs. (48) and (49), and tuning $Z_a^{\rm eff}$ until the resulting pair-potential optimally fits the HNC inversion effective potential in eq. (46) at large x. Examples for systems of colloidal particles with $\sigma_a = \sigma_1 = 250$ nm, suspended at $\varphi_a = \varphi_1 = 10^{-4}$ in an aqueous 1-1 electrolyte with a fixed concentration, $n_3 = 1\ \mu$M, of salt coions, are shown in Figure 7. Results for three different colloidal charge numbers, $Z_1 = 100$, 400, and 1000 are shown. Note that $\chi_3 = \chi_{\rm coion} \gg Z_a\chi_a = Z_1\chi_1$ for all three systems shown in Figure 7, such that the DLVO screening length in eq. (49) is not considerably altered by replacing Z_a with $Z_a^{\rm eff}$. Fitting the potential in eq. (48) to the one obtained from eq. (46) therefore corresponds to vertical translation of $u_{aa}^{\rm DLVO}(x)$ in the linear-logarithmic plot of Figure 7. For the lowest considered colloid charge number, $Z_1 = 100$, the DLVO-potential calculated according to eqs. (48) and (49) (lowermost blue dotted curve) is in nearly perfect agreement with the HNC-inversion potential (lowermost red solid curve). Fitting the DLVO potential with effective charge number input to the HNC-inversion potential, results in $Z_1^{\rm eff} = 99.85$, which is only slightly lower than the bare colloidal charge number. The same procedure, carried out for $Z_1 = 400$ and $Z_1 = 1000$, results in effective charge numbers of $Z_1^{\rm eff} = 390$ and 825, respectively. This demonstrates the capability of the used numerical methods to access HNC solutions of the PM for realistic suspensions of charged colloids, where charge renormalization plays an important role.

In Figure 8, we plot the effective charge of macroions (species 1) as a function of the macroion bare charge, for various concentrations of salt coions, $n_3 = 1$, 10, and 100 μM. The maximal macroion–microion attraction for systems plotted in Figure 8 is characterized by a value of $L_B Z_1/\sigma_1 \approx 3.92$, for $Z_1 = 1400$ and $n_3 = 100\ \mu$M. In agreement with recent small angle X-ray scattering studies for charged colloidal spheres in aqueous electrolytes,[119,120] we find that association of counterions to the macroion surfaces is most efficient at low salinity. This is reflected in Figure 8 by a steepening decay of $Z_1^{\rm eff}(Z_1)$, for decreasing salinity n_3. The macroion–counterion rdf's $g_{12}(x)$ (not shown here) exhibit a contact value $g_{12}(\sigma_{12}n^{1/3}+)$ that is much higher at low than at high salinity, which can be attributed to changes in the effective macroion–counterion pair-potential: in a similar way as the repulsive macroion–macroion interactions, also the attractive macroion–counterion interactions are screened in the presence of (other) microions. This screening is more efficient at high microion concentrations,

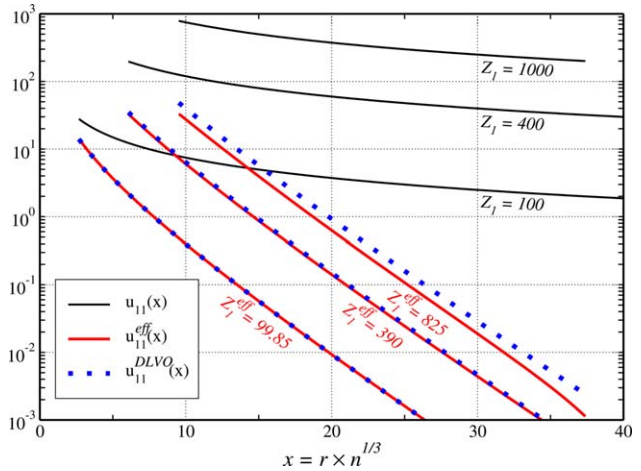

Figure 7. Unscreened dimensionless Coulomb-potentials $u_{11}(x)$ (black solid curves), effective dimensionless pair-potentials $u_{11}^{\rm eff}(x)$, computed by the HNC inversion in eqs. (46) and (47) (red solid curves), and dimensionless DLVO pair potentials $u_{11}^{\rm DLVO}(x)$, defined in eqs. (48) and (49) (blue dotted curves), between a pair of macroions (species 1) in three-component, three-dimensional, globally electroneutral ionic mixtures with common parameters $\sigma_1 = 250$ nm, $\sigma_2 = \sigma_3 = 0.6$ nm, $Z_2 = -1$, $Z_3 = 1$, $L_B = 0.701$ nm, $\varphi_1 = 10^{-4}$, and $n_3 = 1\ \mu$ M. Results for three macroion charge numbers, $Z_1 = 100$, 400, and 1000 are shown. [Color figure can be viewed in the online issue, which is available at wileyonlinelibrary.com.]

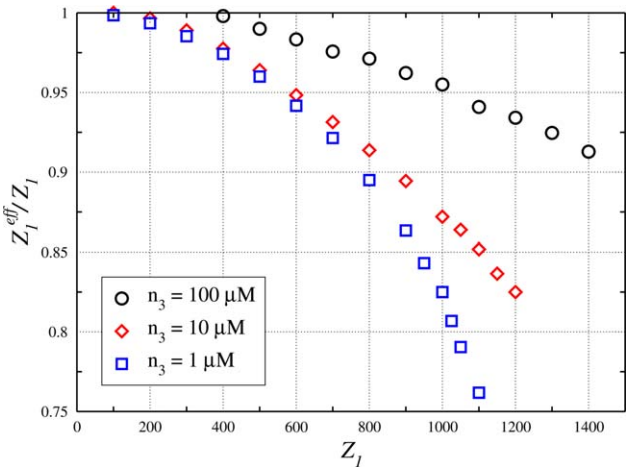

Figure 8. Reduced colloidal effective charge number, Z_1^{eff}/Z_1, as a function of the colloidal bare charge number Z_1, for three-dimensional, globally electroneutral ionic mixtures with counterion concentrations $n_3=100\ \mu$m (black circles), $n_3=10\ \mu$M (red diamonds), and $n_3=1\ \mu$M (blue squares). Common parameters are $\sigma_1=250$ nm, $\sigma_2=\sigma_3=0.6$ nm, $Z_2=-1$, $Z_3=1$, $L_B=0.701$ nm, and $\varphi_1=10^{-4}$. [Color figure can be viewed in the online issue, which is available at wileyonlinelibrary.com.]

that is, at high salinity, where it leads to a less pronounced accumulation of counterions close to the macroion surfaces.

Upon further reducing the salt coion concentration n_3 to values significantly less than 1 μM, we did not succeed in fitting the DLVO potential in eq. (48), with adjustable effective charge number, to the effective potential obtained from the HNC inversion at large particle separations. This failure to predict reliable effective colloidal charge numbers at very low salinity can be traced back to the corresponding small value of the screening parameter k, and the relative long-rangedness of $u_{aa}^{\text{eff}}(x)$: For very long-ranged effective potentials, the asymptotic decay is shifted to particle separations $x\gtrsim 100$, where the LEN condition in eq. (44) is violated due to numerical rounding errors. In such a case, we do not obtain reliable long-ranged asymptotics of $u_{aa}^{\text{eff}}(x)$ from the coupled PM-HNC scheme solution. Unfortunately, the failure of our method to predict effective charges at very low salinity complicates comparisons to CM or RJM results for Z_a^{eff} as a function of Z_a. Although, the CM and RJM are not in principle limited to low salinity,[48] results for $Z_a^{\text{eff}}(Z_a)$ have been published for vanishing or very small salt-ion concentrations only. Note, however, that salt-ion concentrations of less than 1 μM are uncommon in typical experiments where solvent self-dissociation and ionic contaminations such as adsorbed CO_2 are difficult to avoid. The salt concentration range covered in Figure 8, therefore, includes the experimentally most relevant cases. Also, we have checked that our results shown in Figure 8 are in reasonable agreement with modified RJM results for zero salinity and a small volume fraction $\varphi=10^{-3}$, shown in Figure 2 of Ref. 47.

Conclusions

We have shown that a combination of a numerically robust fixed-point iteration scheme and logarithmically spaced computational grids allows efficient computation of HNC solutions of the d-dimensional PM, with explicit results shown for $d \leq 6$. Logarithmic grids are ideally suited for the discretization of pair-correlation functions of ionic mixtures with large particle diameter and charge asymmetries. This has allowed us to access HNC solutions for PM parameters corresponding to realistic suspensions of micrometer-sized colloidal spheres with charge numbers as high as $|Z| \approx 1000$, in an aqueous 1-1 electrolyte.

Numerical stability might be further improved in future studies, if another elaborate fixed-point iteration scheme is used.[75–77,87–89] We expect that this would give access to HNC solutions of the PM at charge and diameter asymmetries exceeding the ones reported here.

We have demonstrated that colloidal effective interaction potentials and effective DLVO charge numbers can be extracted from the multicomponent HNC scheme solution, provided that the salt ion concentration is nonzero, and that the macroion–counterion attraction energy at contact does not exceed a value of $L_B Z_1/\sigma_{11} \approx 4.0$. Our approach of determining colloidal effective charges complements the Poisson-Boltzmann cell model and the jellium model in its various recent modifications. Both the cell model and the jellium model have been solved mostly for vanishing salinity, in very large ranges of the bare colloidal charge Z_1 that exceed the values accessible by our method.

Future projects, based on the methods presented here, might include *ab initio* modeling of colloidal suspensions with reactive electrolytes such as NaOH,[52,53] including chemical association–dissociation reactions influenced by the locally varying pH-value near the colloidal particle's surfaces.

As opposed to MD simulations of the asymmetric PM, with very long program execution times even for moderate ion size and charge-asymmetries, the solution of the HNC equations with the method described here takes few minutes or less on an inexpensive, standard computer. In addition, the HNC is a good approximation for mixtures of charged particles with long-ranged pair-potentials, predicting pair-correlation functions in good agreement with the numerically expensive computer simulations. Despite continuing rapid progress in computer simulations, liquid integral equations therefore remain an indispensable approach in studying highly asymmetric electrolytes.

Acknowledgment

The authors gratefully acknowledge Martin Oettel and Thomas Palberg for helpful discussions.

Keywords: asymmetric electrolytes · colloidal suspensions · liquid integral equations · aqueous solutions · primitive model

How to cite this article: M. Heinen, E. Allahyarov, H. Löwen. *J. Comput. Chem.* **2014**, *35*, 275–289. DOI: 10.1002/jcc.23446

[1] Y. Levin, *Rep. Prog. Phys.* **2002**, *65*, 1577.
[2] J. -P. Hansen, H. Löwen, *Annu. Rev. Phys. Chem.* **2000**, *51*, 209.

[3] R. Messina, *J. Phys. Condens. Matter* **2009**, *21*, 113102.
[4] V. Vlachy, *Annu. Rev. Phys. Chem.* **1999**, *50*, 145.
[5] V. Lobaskin, P. Linse, *J. Chem. Phys.* **1999**, *111*, 4300.
[6] P. Linse, V. Lobaskin, *Phys. Rev. Lett.* **1999**, *83*, 4208.
[7] A.-P. Hynninen, M. Dijkstra, *J. Chem. Phys.* **2005**, *123*, 244902.
[8] E. Allahyarov, H. Löwen, *J. Phys. Condens. Matter* **2009**, *21*, 424117.
[9] L. F. Rojas-Ochoa, R. Castañeda Priego, V. Lobaskin, A. Stradner, F. Scheffold, P. Schurtenberger, *Phys. Rev. Lett.* **2008**, *100*, 178304, ISSN 0031–9007.
[10] R. Castañeda Priego, V. Lobaskin, J. C. Mixteco-Sanchez, L. F. Rojas-Ochoa, P. Linse, *J. Phys. Condens. Matter* **2012**, *24*, 065102, ISSN 0953–8984.
[11] J.-P. Hansen, I. R. McDonald, Theory of Simple Liquids, 3rd ed.; Academic Press: London, **1986**.
[12] T. Morita, *Prog. Theor. Phys.* **1958**, *20*, 920.
[13] C. Caccamo, *Phys. Rep.* **1996**, *274*, 1.
[14] G. Nägele, *Phys. Rep.* **1996**, *272*, 216.
[15] C. Caccamo, G. Pellicane, D. Costa, D. Pini, G. Stell, *Phys. Rev. E* **1999**, *60*, 5533.
[16] G. Zerah, J. -P. Hansen, *J. Chem. Phys.* **1986**, *84*, 2336.
[17] L. Belloni, *J. Chem. Phys.* **1988**, *88*, 5143.
[18] S. Khan, T. L. Morton, D. Ronis, *Phys. Rev. A* **1987**, *35*, 4295.
[19] P. González-Mozuelos, M. D. Carbajal-Tinoco, *J. Chem. Phys.* **1998**, *109*, 11074.
[20] M. D. Carbajal-Tinoco, P. González-Mozuelos, *J. Chem. Phys.* **2002**, *117*, 2344.
[21] L. Belloni, *J. Phys. Condens. Matter* **2002**, *14*, 9323.
[22] J. A. Anta, *J. Phys. Condens. Matter* **2005**, *17*, 7935.
[23] M. Camargo, G. Tellez, *J. Chem. Phys.* **2008**, *128*, 134907.
[24] H. Löwen, P. A. Madden, J. -P. Hansen, *Phys. Rev. Lett.* **1992**, *68*, 1081.
[25] M. Fushiki, *J. Chem. Phys.* **1992**, *97*, 6700.
[26] H. Löwen, J.-P. Hansen, and P. A. Madden, *J. Chem. Phys.* **1993**, *98*, 3275.
[27] D. Léger, D. Levesque, *J. Chem. Phys.* **2005**, *123*, 124910.
[28] H. Löwen, *J. Phys. Condens. Matter* **2001**, *13*, R415.
[29] R. Finken, M. Schmidt, H. Löwen, *Phys. Rev. E* **2002**, *65*, 016108.
[30] J. A. van Meel, D. Frenkel, P. Charbonneau, *Phys. Rev. E* **2009**, *79*, 030201.
[31] J. A. van Meel, B. Charbonneau, A. Fortini, P. Charbonneau, *Phys. Rev. E* **2009**, *80*, 061110.
[32] P. Charbonneau, A. Ikeda, G. Parisi, F. Zamponi, *Phys. Rev. Lett.* **2011**, *107*, 185702.
[33] P. J. Rossky, H. L. Friedman, *J. Chem. Phys.* **1980**, *72*, 5694.
[34] D. G. Gardner, J. C. Gardner, G. Laush, W. W. Meinke, *J. Chem. Phys.* **1959**, *31*, 978.
[35] A. E. Siegman, *J.Opt. Soc. Am. A* **1977**, *1*, 13.
[36] J. D. Talman, *J.Comput. Phys.* **1978**, *29*, 35.
[37] A. J. S. Hamilton, *Mon. Not. R. Astron. Soc.* **2000**, *312*, 257.
[38] A. J. S. Hamilton's, FFTLog website, Available at: http://casa.colorado.edu/~ajsh/FFTLog
[39] J.-M. Caillol, D. Levesque, J. J. Weis, *Mol. Phys.* **1981**, *44*, 733.
[40] J. J. Weis, D. Levesque, J.-M. Caillol, *J. Chem. Phys.* **1998**, *109*, 7486.
[41] Y. V. Kalyuzhnyi, M. Y. Druchok, *J. Mol. Liq.* **2001**, *92*, 97.
[42] Y.-Z. Lin, Y.-G. Li, J.-F. Lu, *J. Chem. Phys.* **2002**, *117*, 407.
[43] T. Kloss, S. M. Kast, *J. Chem. Phys.* **2008**, *128*, 134505.
[44] S. Alexander, P. M. Chaikin, P. Grant, G. J. Morales, P. Pincus, D. Hone, *J. Chem. Phys.* **1984**, *80*, 5776.
[45] E. A. Allahyarov, S. A. Trigger, *High Temp.* **2005**, *43*, 315.
[46] E. Trizac, Y. Levin, *Phys. Rev. E* **2004**, *69*, 031403.
[47] R. Castañeda Priego, L. F. Rojas-Ochoa, V. Lobaskin, J. C. Mixteco-Sánchez, *Phys. Rev. E* **2006**, *74*, 051408, ISSN 1539–3755.
[48] J. Dobnikar, R. Castañeda Priego, H. H. von Grünberg, E. Trizac, *New J. Phys.* **2006**, *8*, 277, ISSN 1367–2630.
[49] T. E. Colla, Y. Levin, E. Trizac, *J. Chem. Phys.* **2009**, *131*, 074115.
[50] J. M. Falcón-González, R. Castañeda Priego, *J. Chem. Phys.* **2010**, *133*, 216101, ISSN 0021–9606.
[51] J. M. Falcón-González, R. Castañeda Priego, *Phys. Rev. E* **2011**, *83*, 041401, ISSN 1539–3755.
[52] D. M. Herlach, I. Klassen, P. Wette, D. Holland-Moritz, *J. Phys. Condens. Matter* **2010**, *22*, 153101.
[53] P. Wette, I. Klassen, D. Holland-Moritz, D. M. Herlach, H. J. Schöpe, N. Lorenz, H. Reiber, T. Palberg, S. V. Roth, *J. Chem. Phys.* **2010**, *132*, 131102.
[54] P. Hopkins, A. J. Archer, R. Evans, *J. Chem. Phys.* **2006**, *124*, 054503.
[55] P. J. Rossky, W. D. T. Dale, *J. Chem. Phys.* **1980**, *73*, 2457.
[56] K.-C. Ng, *J. Chem. Phys.* **1974**, *61*, 2680.
[57] A. R. Allnatt, *Mol. Phys.* **1964**, *8*, 533.
[58] F. Bresme, E. Lomba, J. J. Weis, J. L. F. Abascal, *Phys. Rev. E* **1995**, *51*, 289.
[59] T.-H. Chung, L. L. Lee, *J. Chem. Phys.* **2009**, *130*, 134513.
[60] F. Oberhettinger, Tables of Bessel Transforms; Springer: Berlin, **1972**, ISBN 3-540-05997–0.
[61] P. Pulay, *Chem. Phys. Lett.* **1980**, *73*, 393.
[62] P. Pulay, *J. Comput. Chem.* **1982**, *3*, 556.
[63] T. Rohwedder, R. Schneider, *J.Math. Chem.* **2011**, *49*, 1889.
[64] A. Härtel, M. Oettel, R. E. Rozas, S. U. Egelhaaf, J. Horbach, H. Löwen, *Phys. Rev. Lett.* **2012**, *108*, 226101.
[65] A. Kovalenko, S. Ten-No, F. Hirata, *J.Comput. Chem.* **1999**, *20*, 928.
[66] G. N. Patey, *Mol. Phys.* **1977**, *34*, 427.
[67] N. Hoffmann, C. N. Likos, H. Löwen, *Mol. Phys.* **2007**, *105*, 1849.
[68] J. M. Méndez-Alcaraz, Statische Eigenschaften kolloidaler Suspensionen, Doctorate Thesis, Hartung-Gorre Verlag, Konstanz, **1993**, ISBN 3-89191-655–8.
[69] J. M. Méndez-Alcaraz, R. Klein, *Phys. Rev. E* **2000**, *61*, 4095.
[70] P. González-Mozuelos, J. M. Méndez-Alcaraz, *Phys. Rev. E* **2001**, *63*, 021201.
[71] M. Chávez-Páez, P. González-Mozuelos, M. Medina-Noyola, J. M. Méndez-Alcaraz, *J. Chem. Phys.* **2003**, *119*, 7461.
[72] R. Castañeda Priego, A. Rodríguez-López, J. M. Méndez-Alcaraz, *J. Phys. Condens. Matter* **2003**, *15*, S3393.
[73] C. Contreras-Aburto, J. M. Méndez-Alcaraz, R. Castañeda Priego, *J. Chem. Phys.* **2010**, *132*, 174111.
[74] V. P. Sergiievskyi, M. V. Fedorov, *J.Chem. Theory Comput.* **2012**, *8*, 2062.
[75] M. J. Gillan, *Mol. Phys.* **1979**, *38*, 1781.
[76] S. Labík, A. Malijevský, P. Voňka, *Mol. Phys.* **1985**, *56*, 709.
[77] G. Zerah, *J.Comput. Phys.* **1985**, *61*, 280.
[78] G. Kahl, *Phys. Lett. A* **1988**, *130*, 371.
[79] M. Fushiki, *J. Chem. Phys.* **1988**, *89*, 7445.
[80] F. Thalmann, C. Dasgupta, D. Feinberg, *Europhys. Lett.* **2000**, *50*, 54.
[81] R. Fantoni, G. Pastore, *Phys. Rev. E* **2003**, *68*, 046104.
[82] G. Pastore, R. Santin, S. Taraphder, F. Colonna, *J. Chem. Phys.* **2005**, *122*, 181104.
[83] F. Sausset, G. Tarjus, P. Viot, *J. Stat. Mech. Theory Exp.* **2009**, P04022.
[84] R. Fantoni, A. Giacometti, A. Malijevský, A. Santos, *J. Chem. Phys.* **2009**, *131*, 124106.
[85] P. C. Brandt, A. V. Ivlev, G. E. Morfill, *J. Chem. Phys.* **2010**, *132*, 234709.
[86] J. Puibasset, L. Belloni, *J. Chem. Phys.* **2012**, *136*, 154503.
[87] M. J. Booth, A. G. Schlijper, L. E. Scales, A. D. J. Haymet, *Comput. Phys. Commun.* **1999**, *119*, 122.
[88] C. T. Kelley, B. M. Pettitt, *J.Comput. Phys.* **2004**, *197*, 491.
[89] H. H. H. Homeier, S. Rast, H. Krienke, *Comput. Phys. Commun.* **1995**, *92*, 188.
[90] GSL - GNU Scientific Library, Available at: http://www.gnu.org/software/gsl/.
[91] L. Blum, *J. Chem. Phys.* **1973**, *58*, 3295.
[92] G. N. Patey, *Mol. Phys.* **1978**, *35*, 1413.
[93] P. H. Fries, G. N. Patey, *J. Chem. Phys.* **1985**, *82*, 429.
[94] S. H. L. Klapp, G. N. Patey, *J. Chem. Phys.* **2000**, *112*, 3832.
[95] F. Lado, *J. Chem. Phys.* **1968**, *49*, 3092.
[96] F. Lado, *J.Comput. Phys.* **1971**, *8*, 417.
[97] M. Guizar-Sicairos, J. C. Gutiérrez-Vega, *J.Opt. Soc. Am. A* **2004**, *21*, 53.
[98] D. Hajnal, M. Oettel, R. Schilling, *J. Non Cryst. Solids* **2011**, *357*, 302.
[99] P. Hopkins, M. Schmidt, *J. Phys. Condens. Matter* **2010**, *22*, 325108.
[100] E. Allahyarov, I. D'Amico, H. Löwen, *Phys. Rev. Lett.* **1998**, *81*, 1334.
[101] J. Lekner, *Physica A* **1989**, *157*, 826.
[102] J. Lekner, *Physica A* **1991**, *176*, 485.
[103] M. Mazars, *J. Chem. Phys.* **2001**, *115*, 2955.
[104] P. P. Ewald, *Ann. Phys.* **1921**, *64*, 253.
[105] A. Arnold, C. Holm, In Advanced computer simulation approaches for soft matter sciences II; C. Holm, K. Kremer, Eds.; Advances in Polymer Science, Vol. *185*; Springer-Verlag: Berlin, Germany, **2005**; pp. 59–109, ISBN 3-540-26091–9.
[106] F. J. Rogers, D. A. Young, *Phys. Rev. A* **1984**, *30*, 999.

[107] (a) M. Heinen, P. Holmqvist, A. J. Banchio, G. Nägele, *J. Chem. Phys.* **2011**, *134*, 044532; (b) M. Heinen, P. Holmqvist, A. J. Banchio, G. Nägele, *J. Chem. Phys.* **2011**, *134*, 129901.
[108] E. J. W. Verwey, J. T. G. Overbeek, Theory of the Stability of Lyophobic Colloids; Elsevier: New York, **1948**.
[109] Y. Levin, M. C. Barbosa, M. N. Tamashiro, *Europhys. Lett.* **1998**, *41*, 123.
[110] M. N. Tamashiro, Y. Levin, M. C. Barbosa, *Phys. A* **1998**, *258*, 341.
[111] A. Diehl, M. C. Barbosa, Y. Levin, *Europhys. Lett.* **2001**, *53*, 86.
[112] L. Bocquet, E. Trizac, M. Aubouy, *J. Chem. Phys.* **2002**, *117*, 8138.
[113] E. Trizac, L. Bocquet, M. Aubouy, *Phys. Rev. Lett.* **2002**, *89*, 248301.
[114] E. Trizac, L. Bocquet, M. Aubouy, H. H. von Grünberg, *Langmuir* **2003**, *19*, 4027.
[115] S. Pianegonda, E. Trizac, Y. Levin, *J. Chem. Phys.* **2007**, *126*, 014702.
[116] A. Torres, G. Tellez, R. van Roij, *J. Chem. Phys.* **2008**, *128*, 154906.
[117] M. G. McPhie, G. Nägele, *Phys. Rev. E* **2008**, *78*, 060401.
[118] H. Ohshima, T. W. Healy, L. R. White, *J.Colloid Interface Sci.* **1982**, *90*, 17.
[119] F. Westermeier, B. Fischer, W. Roseker, G. Grübel, G. Nägele, M. Heinen, *J. Chem. Phys.* **2012**, *137*, 114504.
[120] K. van Gruijthuijsen, M. Obiols-Rabasa, M. Heinen, G. Nägele, A. Stradner, Langmuir **2013**, *29*, 11199.

Received: 15 July 2013
Revised: 3 September 2013
Accepted: 9 September 2013
Published online on 9 October 2013